PAPER

Check for updates

Electrochemical reduction of NO catalyzed by boron-doped C_{60} fullerene: a first-principles study†

Nasibeh Saeidi,[a] Mehdi D. Esrafili [ID] *[b] and Jaber Jahanbin Sardroodi [ID] [a]

The electrochemical reduction of nitrogen monoxide (NO) is one of the most promising approaches for converting this harmful gas into useful chemicals. Using density functional theory calculations, the work examines the potential of a single B atom doped C_{60} fullerene ($C_{59}B$) for catalytic reduction of NO molecules. The results demonstrate that the NO may be strongly activated over the B atom of $C_{59}B$, and that the subsequent reduction process can result in the formation of NH_3 and N_2O molecules at low and high coverages, respectively. Based on the Gibbs free energy diagram, it is inferred that the $C_{59}B$ has excellent catalytic activity for NO reduction at ambient conditions with no potential-limiting. At normal temperature, the efficient interaction between the *NOH and NO species might lead to the spontaneous formation of the N_2O molecule. Thus, the findings of this study provide new insights into NO electrochemical reduction on heteroatom doped fullerenes, as well as a unique strategy for fabricating low-cost NO reduction electrocatalysts with high efficiency.

1. Introduction

The continual growth in the concentration of hazardous air pollutants is one of the most pressing concerns in today's modern world. Nitric monoxide (NO) is a main environmental pollutant generated by the burning of fossil fuels in different industrial processes and internal combustion engines.[1,2] NO species in the atmosphere can interact with water molecules, resulting in acid rain, which has a detrimental impact on plants, forests, soil, buildings, and human health. Additionally, NO contributes to photochemical smog and ozone depletion.[3] High NO concentrations can cause a variety of health issues in humans, including irritation of the eyes, nose, and mucous membranes. Hence, controlling NO emission and minimizing the atmospheric concentration of this toxic gas are critical to protect public health and the environment.[4,5] Several effective ways for eliminating NO molecules from waste gases have been presented to achieve this goal.[6–10] Recent studies, for example, have demonstrated that in the presence of visible light radiation, NO molecules may be readily oxidized over chemically doped TiO_2 (ref. 9) and SnO_2 (ref. 10) photocatalysts. The insertion of Fe (Ce) atoms in TiO_2 (SnO_2) was revealed to result in the formation of oxygen vacancies, which further facilitated NO deep oxidation under visible light irradiation.

Electrochemical techniques are one of the most effective methods for addressing environmental and energy issues. Clearly, converting hazardous NO directly to NH_3 *via* an environmentally friendly electrocatalytic reduction process not only prevents NO pollution, but the resultant product may also be used in industry. In the electrocatalytic reduction process, the type and nature of the catalyst is an important factor in improving reaction rate, lowering energy consumption and costs, and enhancing reaction selectivity.[11] For the NO electrochemical reaction (NOER), different pure transition metals (TMs) such as Cu, Pt, Pd, and other electrocatalysts have been commonly employed.[12–14] Although these metal surfaces have a high catalytic activity for NOER, the low utilization of atoms and poor long-term stability have limited their industrial applicability. As a result, it is critical to look for low-cost, high-efficiency alternative NOER electrocatalysts.

In recent years, single-atom catalysts (SACs) have emerged as a distinct branch of heterogeneous catalysts due to their high metal performance and long-term durability.[15–18] SACs are also promising candidates for addressing the poor atom efficiency issues of bulk metals and metal clusters used in various electrocatalytic processes such as N_2 fixation,[19,20] O_2 (ref. 21) and CO_2 (ref. 22 and 23) reduction or hydrogen evolution reaction (HER).[24,25] Numerous studies[26–28] based on density functional theory (DFT) have also demonstrated the potential of such SACs for electrochemical NO molecule reduction. Wang *et al.*[26] investigated the NO binding on various TM doped nitrogen incorporated graphene (TM = Sc–Cu, Mo, Rh, and Ru) and found that the Co atom is the most suitable SAC for the reduction of NO. Furthermore, their DFT calculations revealed that the following NOER process can generate either NH_3 or

[a]Department of Chemistry, Azarbaijan Shahid Madani University, Tabriz, Iran
[b]Department of Chemistry, Faculty of Basic Sciences, University of Maragheh, P. O. Box 55136-553, Maragheh, Iran. E-mail: esrafili@maragheh.ac.ir
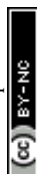
N_2O on the embedded CoN_4 moiety, depending on the coverage of the NO molecules. Aside from the fact that the nature of the doped TM atom can influence the activation of the N–O bond of NO molecule, the geometry and electronic structure of the utilized support would have a significant impact on the catalytic activity and selectivity of the SACs.[29] Generally, the defect-free supports are assumed to be intact to stabilize the deposited TM atoms. However, introducing various defect sites or chemical doping with heteroatoms might be a helpful approach for improving support-metal interaction and regulating the positive charge on the TM atom.[30,31]

Carbon nanostructures like fullerenes, nanotubes, and graphene have gained a lot of interest in the recent decade due to their unique chemical and physical characteristics.[32–37] Buckminsterfullerene (C_{60}) is an important member of the carbon fullerenes, composed of twenty six-membered and twelve five-membered carbon atom rings with sp^2 hybridization. Because of its outstanding physicochemical characteristics and highly symmetrical structure, C_{60} and its derivatives are used in a number of applications, including hydrogen storage,[38,39] solar cells,[40,41] light emitting diodes[42] and drug delivery.[43–45] C_{60} may serve as both an electron donor and acceptor, and it can be used to detect and recognize dangerous gas molecules.[46–48] Furthermore, chemical doping of heteroatoms like N, B, and Si into the C_{60} can result in significant structural and electronic deformation, causing to significant changes in its charge distribution, thermal stability, Fermi level, and band gap.[49–51] For example, carbon-π electrons can be effectively activated by the insertion of a B atom into C_{60} because of charge transfer between B and its surrounding C atoms.[52,53] Consequently, $C_{59}B$ may adsorb small gas molecules such as O_2, CO, and N_2O due to the buildup of high spin density and relatively large positive charges over the B atom.[53–55] Likewise, the metal-free $C_{59}B$ is expected to be a very active catalyst for NO adsorption and electrochemical reduction. However, no theoretical or experimental studies on the catalytic reactivity of $C_{59}B$ for the NOER process have been conducted.

The aim of this investigation is to provide theoretical insights into the NOER mechanism over $C_{59}B$ fullerene. This study particularly addresses the following questions based on the DFT calculations: (1) how feasible is the using of the metal-free $C_{59}B$ electrocatalyst to reduce NO electrochemically? (2) What role does the B atom play in the catalytic activity of $C_{59}B$? (3) Is it possible to use this electrocatalyst for NOER at room temperature?, and (4) Is the proposed $C_{59}B$ electrocatalyst selective for the NOER in the presence of the competing HER process? The findings of this work might help in the design and manufacture of highly active and low-cost NOER electrocatalysts based on carbon fullerenes.

2. Theoretical simulations

All geometry optimizations and electronic structure calculations were conducted by the DMol.[3,56,57] The exchange-correlation effects were taken into account by the Perdew–Burke–Ernzerhof (PBE)[58,59] density functional. The weak van der Waals interactions between adsorbates and $C_{59}B$ electrocatalyst

were included using the Grimme's DFT+D2 scheme.[59] A double numerical plus polarization function (DNP) basis set and the smearing value of 0.005 Ha were then specified in all calculations. The global orbital cut-off was determined to be 4.6 Å. The convergence thresholds were set to 10^{-5} Ha for energy, 0.001 Ha $Å^{-1}$ for maximum force, and 0.005 for maximum displacement during the geometry optimization. To investigate the charge transfer in various species, the Hirshfeld charge population analysis[60] was performed. There were no symmetry constraints during the structural optimization.

For the DFT computations, a cubic box with dimensions $a = b = c = 25$ Å was utilized. To prepare the $C_{59}B$ electrocatalyst, a C atom was replaced with a B atom in the C_{60} structure. The formation energy (E_{form}) of $C_{59}B$ was computed to evaluate its stability according to the following equation:

$$E_{form} = E_{C_{59}B} + \mu_C - E_{C_{60}} - \mu_B \quad (1)$$

here, $E_{C_{59}B}$ and $E_{C_{60}}$ are total energies of $C_{59}B$ and C_{60}, respectively. μ_C refers to the energy of one carbon atom in the pristine C_{60} and μ_B is the chemical potential of a B atom in its most stable crystalline form. According to the above definition, a negative E_{form} shows that $C_{59}B$ formation is favorable from a thermodynamically point of view. To evaluate the stability of each adsorbed species (X) on the $C_{59}B$ electrocatalyst, the adsorption energy (E_{ads}) was calculated by

$$E_{ads} = E_{X/C_{59}B} - E_{C_{59}B} - E_X \quad (2)$$

Here, $E_{X/C_{59}B}$, $E_{C_{59}B}$ and E_X refer to the energies of the adsorbate/substrate complex, isolated $C_{59}B$ and adsorbate molecules, respectively.

The computational hydrogen electrode (CHE) model developed by Nørskov and coworkers[61] was used to investigate the electrochemical process. According to this approach, the Gibbs free energy (G) of a proton–electron pair (H^+/e^-) is equivalent to one-half of the free energy of an H_2 molecule. The change in the Gibbs free energy (ΔG) was calculated for each reduction step using

$$\Delta G = \Delta E + \Delta E_{ZPE} - T\Delta S + \Delta G_{pH} + \Delta G_U \quad (3)$$

Here, ΔE refers to the reaction energy, which is directly obtained from the DFT total energies at 0 K. For instance, the ΔE of NO adsorption over $C_{59}B$ could be characterized as

$$\Delta E = E_{NO/C_{59}B} - E_{C_{59}B} - E_{NO} \quad (4)$$

in which, $E_{NO/C_{59}B}$, E_{NO}, and $E_{C_{59}B}$ correspond to the total energies of $NO/C_{59}B$ complex, pristine $C_{59}B$ and isolated NO molecule, respectively. ΔE_{ZPE} and ΔS are the changes in zero-point energy and entropy computed from vibrational frequencies at 298.15 K. The entropies and zero-point energies of free NO, H_2O, N_2O, and NH_3 molecules were obtained from the NIST database.[62] ΔG_{pH} which is represented as $\Delta G_{pH} = k_B T \times pH \times \ln 10$, is the pH free energy correction. In the latter equation, k_B is the Boltzmann constant and pH = 0 is considered for the acidic medium. The ΔG_U term denotes the effect of the potential

U on the system. The limiting potential (U_{L}) for each pathway was calculated from the maximum free energy change (ΔG_{max}) using the equation $U_{\mathrm{L}} = -\Delta G_{\mathrm{max}}/e$. All DFT computations were carried out in a water solvent using the conductor-like screening model (COSMO)[63] as implemented in DMol.[3]

The ΔG value of the competing HER process was obtained by the following equation:[64]

$$\Delta G = \Delta E_{\mathrm{H}} + 0.24 \ (\text{in eV}) \tag{5}$$

in which ΔE_{H} is the reaction energy acquired by adsorption of a H atom on the $C_{59}BH$ which can be obtained by

$$\Delta E_{\mathrm{H}} = E_{C_{59}BH} - E_{C_{59}B} - \tfrac{1}{2}(E_{H_2}) \tag{6}$$

where $E_{C_{59}BH}$ and $E_{C_{59}B}$ are the energies of the $C_{59}BH$ and $C_{59}B$ systems, respectively, and E_{H_2} is the energy of an H_2 molecule, all within the water phase.

3. Results and discussion

3.1 $C_{59}B$ electrocatalyst

To understand the NOER mechanism over the $C_{59}B$ electrocatalyst, the geometry and electronic structure of $C_{59}B$ must first be addressed. The relaxed structures of pristine and B-doped C_{60} fullerenes as well as their density of states (DOS) plots are shown in Fig. 1. Because all of the carbon atoms in the C_{60} structure are symmetrically equivalent, there is only one way to incorporate a B atom into C_{60} to create the $C_{59}B$ structure. Doping of the B atom resulted in a small distortion around the dopant atom, which is consistent with the prior studies.[55,65,66] As seen in Fig. 1, the C–C bond lengths surrounding the dopant atom are nearly equal to those of pure C_{60}. This is due to the fact

that the B atomic radius is nearly identical to that of the C atom. Furthermore, the triple-coordination feature of the B atom enables it to be readily inserted in the C_{60} structure. The B–C bond distances in $C_{59}B$ shared by two neighboring hexagons and the hexagon and pentagon rings are calculated to be 1.53 and 1.55 Å, respectively, which agree well with the other findings.[53,54] According to eqn (1), $C_{59}B$ has a negative formation energy (-5.23 eV), suggesting that the B atom is well integrated into the C_{60} network. This negative value is also consistent with those found in previous DFT investigations,[67–69] thus indicating that the $C_{59}B$ is thermodynamically stable. The insertion of the B atom into the C_{60} can result in electron density redistribution, particularly near the dopant atom. The B atom in $C_{59}B$ is positively charged by $0.10|e|$, whereas each surrounding carbon atom has a negative charge of $0.06|e|$. The DOS plots of the C_{60} and $C_{59}B$ fullerenes are shown in Fig. 1. The significant hybridization between the 2p orbitals of the B atom and those of adjacent C atoms should be the origin of the covalent B–C bonds in $C_{59}B$. These findings, along with the substantial negative formation energy, ensure that $C_{59}B$ is very stable and may thus be utilized as a robust electrocatalyst for NO molecule reduction.

3.2 Adsorption of NO over $C_{59}B$

Since NO adsorption is regarded as a critical step in the NOER process, we then consider the adsorption behavior of this molecule on $C_{59}B$. To this end, several initial adsorption configurations are thoroughly investigated, including those in which NO approaches the B or C atoms of $C_{59}B$ from its N or O sites (end-on) as well as from the N–O bond (side-on). The optimized adsorption structures, as well as the partial DOS (PDOS) plots and electron density difference ($\Delta\rho$) maps, are
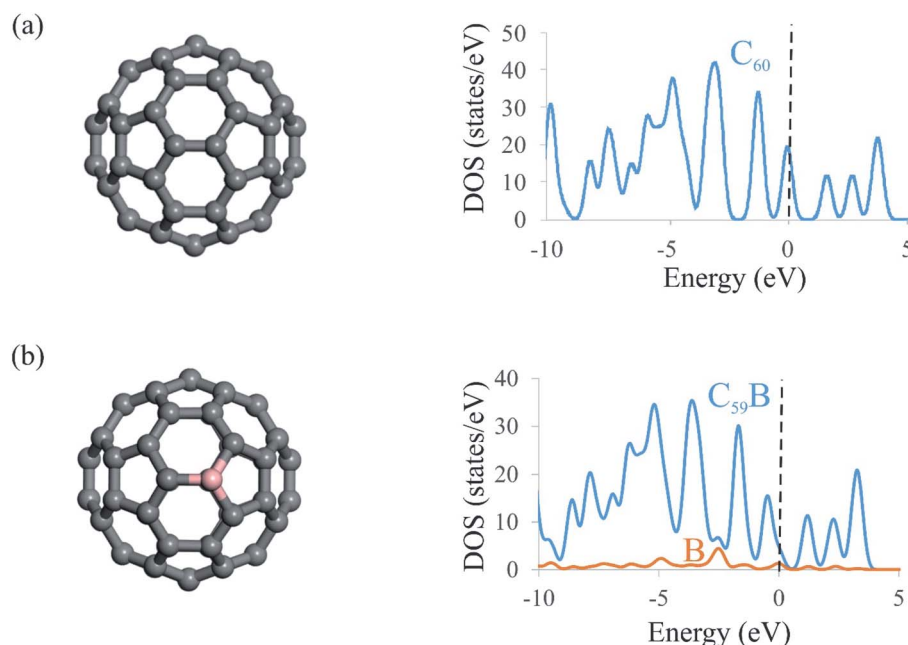

Fig. 1 Optimized structures and DOS plots of (a) C_{60} and (b) $C_{59}B$. The dashed line at $E = 0$ in DOS plots shows the Fermi level.

depicted in Fig. 2. As can be observed, the NO molecule can be adsorbed onto the B atom of $C_{59}B$ through its N (complex **C1**) or O atoms (complex **C2**). The NO molecule is tilted over the $C_{59}B$ substrate in both configurations, with B–N and B–O bonding lengths of 1.73 and 2.42 Å, respectively. The calculated adsorption energy (E_{ads}) values for the attachment of NO from its N atom is −0.93 eV, which is 0.71 eV more negative than that of from the O atom (Table 1). This indicates that the NO molecule is preferentially bonded to the B atom through the N atom. The charge analysis based on the Hirshfeld method shows that the formation of **C1** and **C2** complexes is associated with a shift of 0.13 and 0.35 electrons from the $C_{59}B$ surface into NO, respectively. In the adsorbed structures, the N–O bond distance is calculated to be 1.18 (**C1**) and 1.13 Å (**C2**), deviating slightly from the N–O bond of the isolated NO (1.16 Å). According to Table 1, the changes in the Gibbs free energy (ΔG_{ads}) due to the adsorption of the NO *via* its N and O sites are

Table 1 Adsorption energy (E_{ads}), adsorption Gibbs free energy (ΔG_{ads}, at 298 K and 1 atm) and net charge-transfer (q_{CT}) for NO adsorption over $C_{59}B$

Adsorbate	E_{ads} (eV)	ΔG_{ads} (eV)	q_{CT} (e)
NO (N-site)	−0.93	−0.21	0.13
NO (O-site)	−0.22	0.50	0.35

−0.21 and 0.50 eV, respectively. This means that, unlike **C1**, the formation of **C2** is not possible at room temperature due to entropic effects. The PDOS analysis of **C1** and **C2** complexes reveals a remarkable mixing of the singly-occupied $2\pi^*$ states of NO and the empty 2p state of the B. It can be also observed that the amount of such orbital hybridization in the complex **C1** is more significant than **C2**, which is compatible with the E_{ads} values previously stated. Furthermore, the $\Delta\rho$ maps in Fig. 2
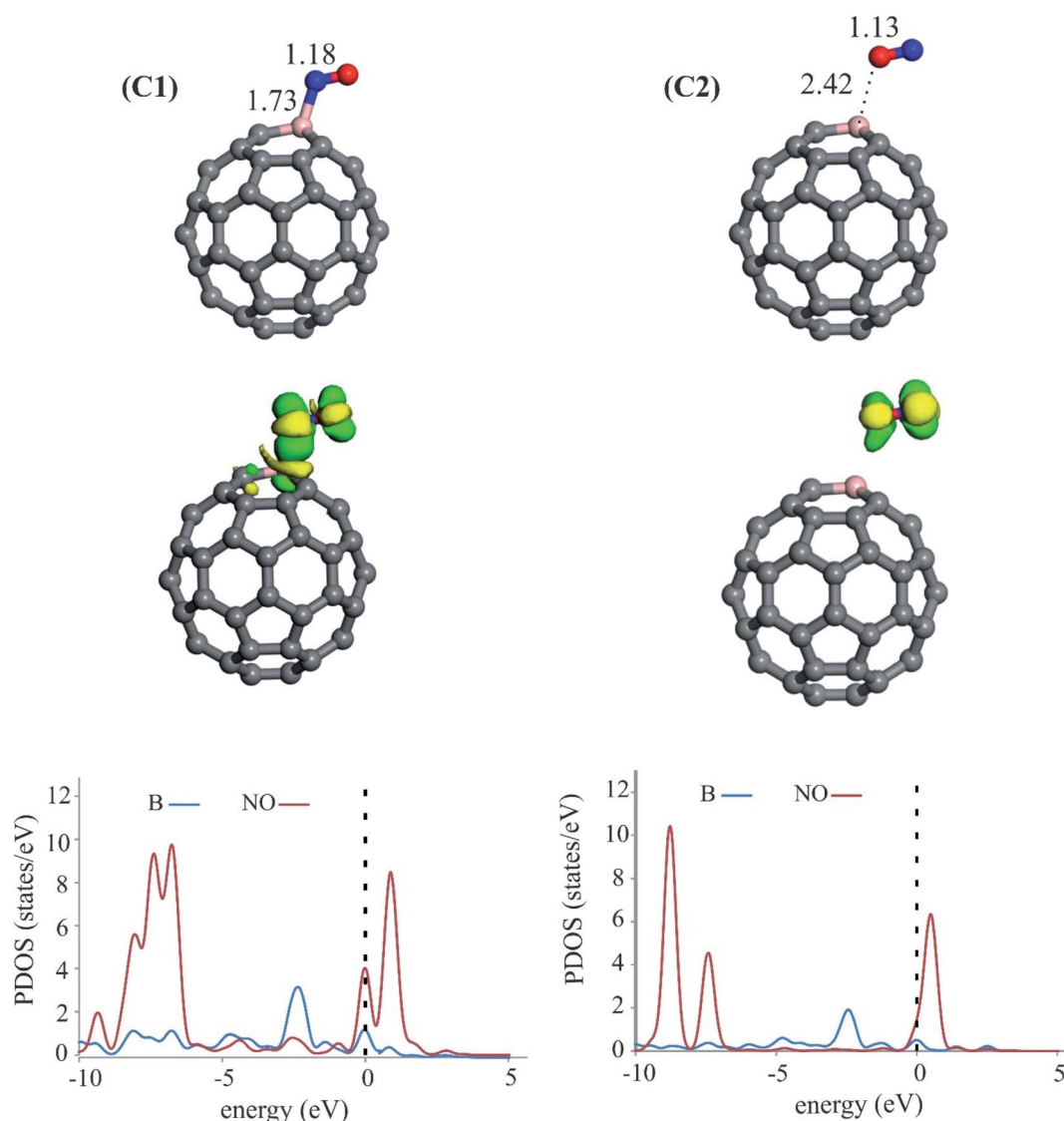

Fig. 2 Optimized structures (above) with their $\Delta\rho$ isosurface (isovalue = 0.03 au, middle) and PDOS plots (below) of **C1** and **C2** complexes. In the $\Delta\rho$ plots, the charge depletion and accumulation sites are displayed in green and yellow, respectively. All bond distances are in Å.

show that there is a substantial buildup of electron density over the NO, whereas an electron density depletion region appears over the B atom. Clearly, the degree of electron density redistribution correlates well with the adsorption strength of NO molecule in **C1** and **C2** complexes. In other words, $\Delta\rho$ is more pronounced for **C1** than in **C2**. According to these results, NO adsorption from its N-site is more energetically favorable than its O-site. This indicates that when exposed to $C_{59}B$, the N atom of NO easily attaches to the B atom, activating the N–O bond for the subsequent NOER process.

The adsorption of NO on the carbon atoms of $C_{59}B$ is also investigated, and it is revealed that NO is preferentially adsorbed through its N site. Fig. S1 of the ESI† displays the optimized structure of the two most stable configurations (complexes **C3** and **C4**). As can be seen, the E_{ads} value is modest in both cases, suggesting that NO adsorption over the C atoms of C_{59} is less likely. Furthermore, for these adsorption configurations, the ΔG_{ads} is positive. The PDOS analysis also confirms the physisorption of NO over the C atoms of $C_{59}B$, where there exist weak hybridizations between the electronic states of NO and $C_{59}B$. As a result, the B atom of C_{59} is the most favorable site for NO molecule adsorption.

3.3 NOER process

Previous studies[13,70] have found that the concentration of NO molecules determines the most energetically favorable route and the final products of the NOER process. While NH_3 is the major product at low NO coverage, N_2O is the most favorable product at high NO coverage. As a result, we investigate the NOER process at both low and high NO coverages. However, before discussing the NOER process, the addition of H^+ and e^- to pre-adsorbed NO molecule must be examined separately, since recent studies have revealed that they may play a key role in the NO activation on photocatalysts.[9,10] Fig. 3a and b show the optimized structure of the NOH^+ and NO^- adsorption configurations, respectively. According to our findings, the E_{ads} value of NOH^+ is −5.31 eV, which is considerably higher (more negative) than that of NO^- (−4.62 eV). It should be noted that protonation of NO causes the B–C bond of $C_{59}B$ to be broken and the N atom of NO to be inserted between the B and C atoms. Furthermore, the E_{ads} value for the adsorption of NOH^+ and

NO^- species is substantially larger than that of neutral NO. This can be ascribed to the stability of the 5σ and $2\pi^*$ states of NO, facilitating charge transfer between this molecule and $C_{59}B$.

3.3.1 NOER process under low NO coverage. The reaction pathways for the electrochemical reduction of NO to NH_3 are shown in Fig. 4a. The H^+/e^- pairs are sequentially added to the adsorbed species to locate the minimum energy structures in each hydrogenation step. As can be seen, the activated NO molecule (*NO) is hydrogenated in the first step by an H^+/e^- pair. To assess the NOER performance of the $C_{59}B$ substrate, two potential hydrogenation reaction pathways (P1 and P2) may be examined. In pathway P1, the first hydrogen atom is attached to the O atom of the *NO molecule, resulting in the *NOH species, whereas in pathway P2, the *HNO moiety is produced by adding the hydrogen atom to the N atom of the *NO molecule. For the hydrogenation of *NOH and *HNO moieties, two pathways may be considered; they are denoted by P1-1, P1-2 for the pathway P1 and P2-1, P2-2 for the pathway P2, respectively (see Fig. 4a). Fig. 5 depicts the relaxed geometries of different chemical intermediates involved in the four described routes and related ΔG and ΔE values.

3.3.1.1 P1-1 pathway. The ΔG and ΔE values for each hydrogenation step of P1-1 pathway are shown in Fig. 5. Fig. S2 and S3† also depict the variation of ΔG and ΔE values during the NO reduction process, respectively. The N–O bond distance in the *NOH intermediate is calculated to be 1.42 Å, which is 0.26 Å larger than that of isolated NO. Furthermore, the binding distance between the B atom and *NOH is 1.50 Å, which is less than that found for *NO. The ΔE and ΔG values for obtaining *NOH are −1.02 and −0.59 eV, respectively, suggesting that this process is exothermic and thermodynamically feasible. In step 2, the O atom of *NOH is further hydrogenated to yield the H_2O molecule, while the *N species remains over the B atom of the electrocatalyst with a *N–B bond distance of 1.43 Å. The reaction energy for this step is −0.88 eV, whereas the Gibbs free energy of the system is lowered by 1.31 eV owing to the detachment of the H_2O molecule. After the H_2O molecule is released, the third hydrogen is added to the remaining *N moiety, forming the *NH intermediate with ΔG and ΔE values of −1.25 and −1.65 eV, respectively. Continuous hydrogenation yields a *NH_2 intermediate with the ΔE value of −1.40 eV. The associated free energy change of this step is −1.01 eV, according to Fig. 5. In the next step, *NH_2 is hydrogenated to *NH_3 molecule on top of the $C_{59}B$ substrate. This ΔE and ΔG values of this step are −0.91 and −0.56 eV, respectively. Lastly, because of its low free energy (−0.01 eV), the produced NH_3 can be easily separated from the B atom.

3.3.1.2 P1-2 pathway. In pathway P1-2, the second hydrogen attaches the N atom of the *NOH and forms the *HNOH moiety. As indicated in Fig. 5, ΔG and ΔE values for this step are −0.23 and −0.57 eV, respectively. Note that the ΔG value for *HNOH formation is 1.08 eV smaller than that of *N species (−1.31 eV), making *HNOH formation less favorable. The addition of hydrogen atom to *NOH also causes the B–N bond elongate from 1.50 to 1.56 Å. The introduction of the third H^+/e^- pair then converts *HNOH into *NH and H_2O species with a large negative ΔG value (−2.33 eV). The calculated ΔE of this step is
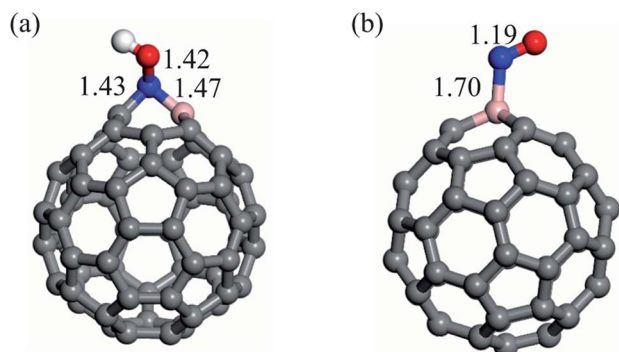

Fig. 3 The adsorption configuration of (a) NOH^+ and (b) NO^- over $C_{59}B$. Bond distances are in Å.
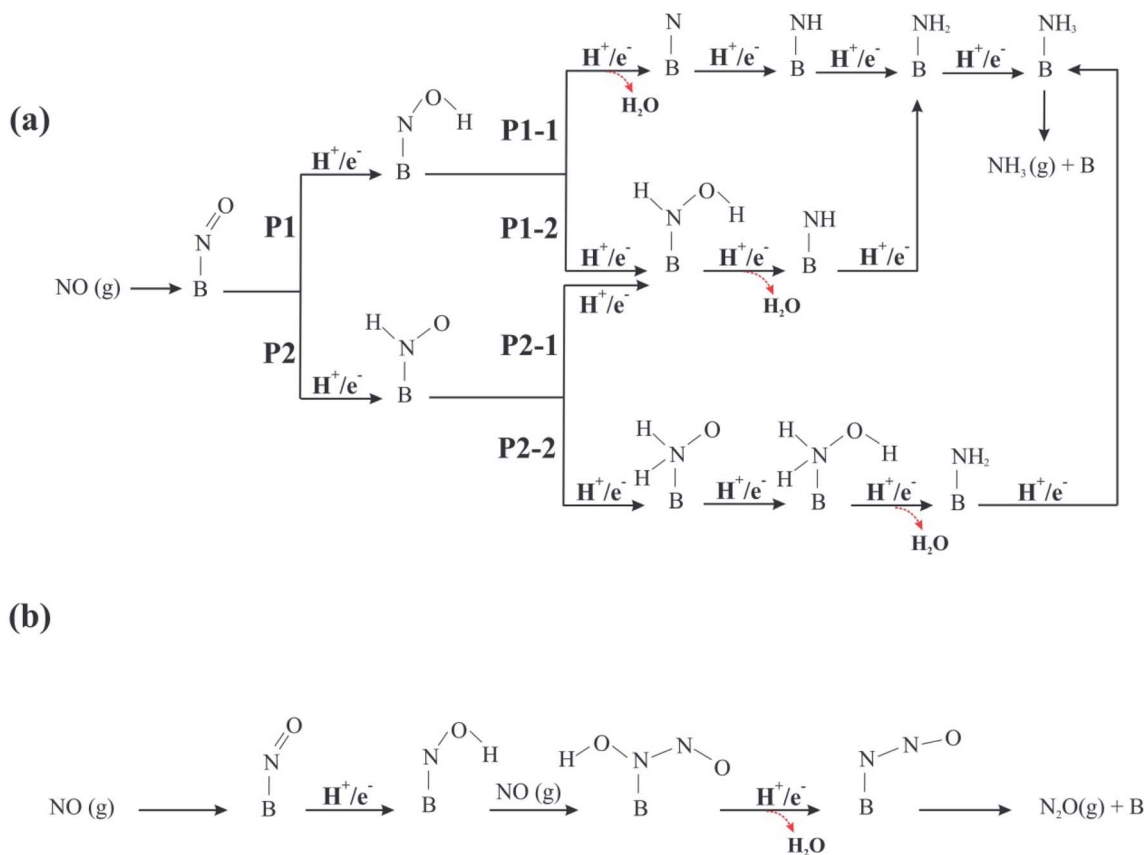
Fig. 4 Schematic representation of possible reaction pathways for NOER process over $C_{59}B$ at (a) low and (b) high NO coverage.

−1.96 eV. Upon the attachment of the fourth hydrogen to the *NH intermediate, the *NH_2 moiety is produced. The calculated ΔG and ΔE values for step 4 of the pathway are −1.01 and −0.91 eV, respectively. The hydrogenation process is continued in Fig. 4a in a way similar to that of pathway P1-1, and ΔG and ΔE have the same values (Fig. 5). Overall, comparing the free energy values acquired *via* the P1-1 and P1-2 clearly demonstrates that the former route is favored over the latter. This might be owing to the fact that the formation of the *N + H_2O species (−1.31 eV) is more energetically favorable than the formation of *HNOH (−0.23 eV).

For the NOER through the P2 pathway, the N atom of the *NO species is hydrogenated by adding an H^+/e^- pair, and *HNO is produced over the $C_{59}B$ electrocatalyst. The B–N, N–O, and N–H bond lengths in the *HNO are 1.55, 1.24, and 1.04 Å, respectively, which are comparable to the B–N (1.50 Å), N–O (1.42 Å), and O–H (0.98 Å) bond lengths in the *NOH moiety. This step has a reaction energy of −0.91 eV and a free energy change of −0.51 eV. From a thermodynamic standpoint, the *NOH intermediate is preferable to the *HNO; hence, the *NOH is an important intermediate in the NOER process (Fig. S2 and S3 of ESI†). As shown in Fig. 4a, the *HNO intermediate can be hydrogenated *via* its O-site or N-site, and NOER can proceed by two distinct routes, P2-1 and P2-2.

3.3.1.3 P2-1 pathway. When the NOER proceeds through the P2-1 pathway, the second H^+/e^- pair is attached to the O atom of

*HNO, giving the *HNOH with a ΔG value of −0.31 eV. In addition, the ΔE value corresponding to this step is −0.68 eV. The N–O and B–N bonds distances are calculated to be 1.38 and 1.57 Å, respectively. By continuing the reaction and reaching step 3, the O atom is hydrogenated with the third hydrogen, resulting in the formation of the H_2O molecule. This corresponds to a release of 1.96 eV energy, whereas the Gibbs free energy of the system is lowered by 2.33 eV. As shown in Fig. 4a, the NH_3 molecule is formed by successive hydrogenation of the remaining *NH moiety, with these steps being similar to those in the P1-2 route. The corresponding ΔG and ΔE values are shown in Fig. 5.

3.3.1.4 P2-2 pathway. In pathway P2-2, the N atom of *HNO is first hydrogenated to form *H_2NO species. The free energy of the system increases by 0.07 eV, whereas about 0.30 eV energy releases in this step. The hydrogenation of the *H_2NO in the next step results in the formation of the *H_2NOH moiety with a free energy change of −1.03 eV. This reaction step is also exothermic, with ΔE = −1.78 eV. The addition of another H atom to *H_2NOH can then lead to formation of *NH_2 and H_2O species. This step releases a significant amount of energy (1.93 eV), with the associated large free energy change (−2.69 eV). Finally, hydrogenation of the *NH_2 yields the *NH_3 molecule, whose ΔG and ΔE values are similar to those of the other three previously described routes (Fig. 5). The second hydrogenation in the P2-2 route is endothermic, whereas the other elementary
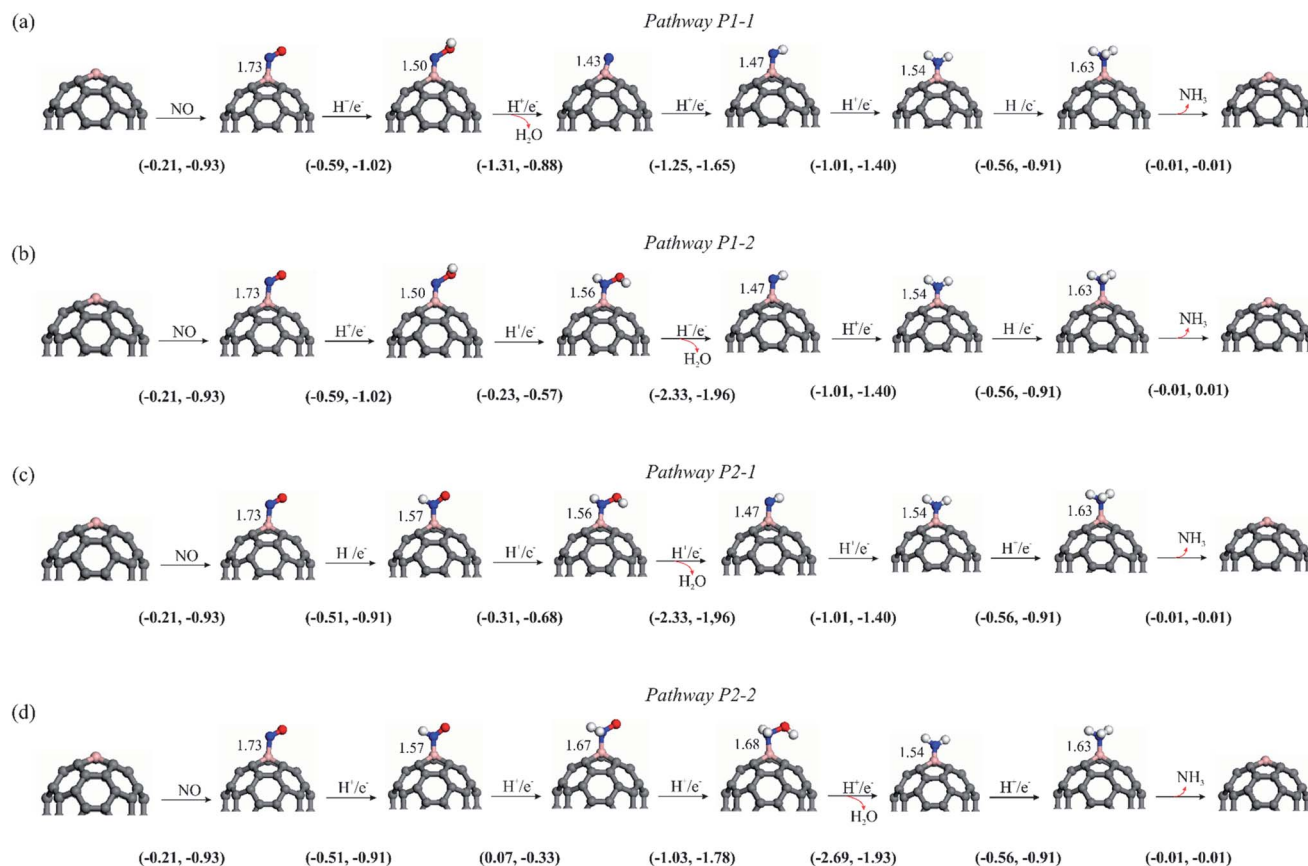
Fig. 5 Optimized structure of various intermediates for NOER to NH_3 along the (a) P1-1, (b) P1-2, (c) P2-1 and (d) P2-2 pathways over $C_{59}B$. All B−N bond distances are in Å. The first number in the parentheses is the ΔG, while the second is the ΔE.

steps are exothermic. As a result, $*H_2NO$ formation might be considered as the potential-limiting step. The corresponding U_L value is much lower than that of the NOER on the B-graphene,[71] Si–N$_4$/graphene,[28] Co–N$_4$/graphene[70] and Cu decorated g-C$_3$N$_4$.[72] Furthermore, a comparison of the P2-1 and P2-2 routes indicates that the ΔG and ΔE values due to the formation of $*H_2NO$ (+0.07 and −0.33 eV) are significantly smaller than those of $*HNOH$ (−0.31 and −0.68 eV); hence, formation of the $*HNOH$ is more favorable from an energy viewpoint.

As shown in Fig. 5, the ΔG value for all reaction steps involved in the P1 pathway is negative. Also, the formation of the water molecule in the P1-2 channel is associated with the largest (more negative) ΔG. Except for the $*H_2NO$ formation in P2-2, the ΔG value for each reaction step in the P2 pathway is

negative. This indicates that the latter step cannot take place under normal conditions. Furthermore, because the first hydrogenation step of $*NO$ is crucial in initiating the NO reduction, the ΔG values of both processes are compared. The ΔG value for the first hydrogenation step of $*NO$ via the P1 route is found to be slightly more negative than that of P2. This indicates that the formation of the $*HNO$ moiety is more thermodynamically favorable than that of the $*NOH$. As a result, the NOER should proceed through $*HNO$ formation, and the P1 would be the primary reaction route to generate NH_3 molecules over the $C_{59}B$ catalyst.

3.3.2 NOER process under high NO coverage. As the concentration of NO molecules increases over the catalyst, the final product of the NOER process is the N_2O molecule rather
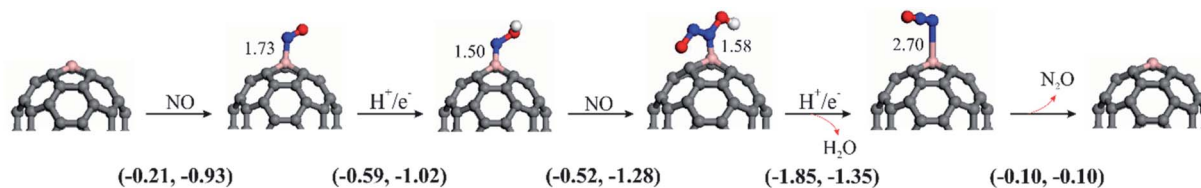

Fig. 6 Optimized structures of NOER species over $C_{59}B$ at high NO coverage. All B−N bond distances are in Å. All B−N bond distances are in Å. The first number in the parentheses is the ΔG, while the second is the ΔE.
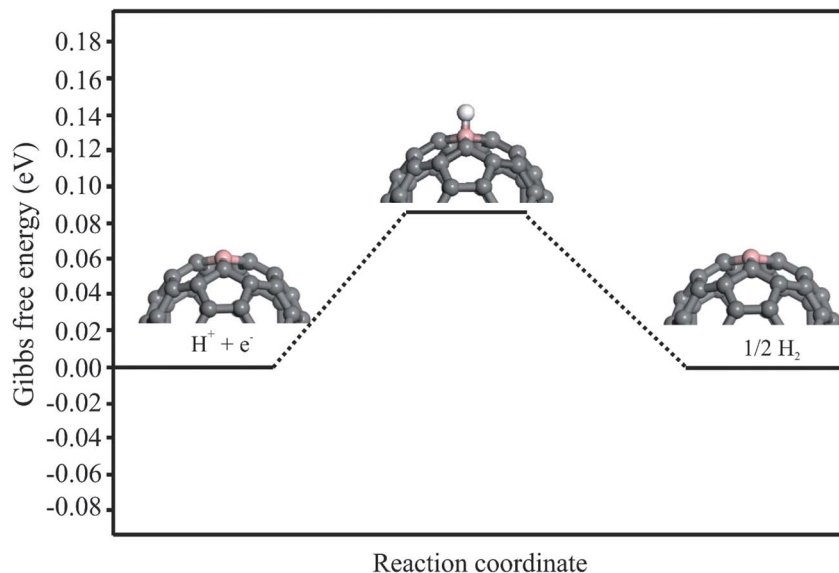
Fig. 7 The Gibbs free-energy diagram of HER under standard conditions over $C_{59}B$.

than the NH_3. Fig. 6 depicts the relaxed structures involved in the NOER process at high NO coverage, and the related ΔE and ΔG values. The ΔE and ΔG profiles are shown in Fig. S4.† Coupling between the N atoms of the *NOH and NO species results in the formation of the *NOHNO intermediate, and the free energy is lowered by 0.52 eV during this step (Fig. 6). The B–N bond length is 1.58 Å in comparison to that of adsorbed *NOH (1.50 Å), while the bonding distance of N–N is 1.26 Å. Following that, the O atom of the OH moiety in *NOHNO intermediate is hydrogenated, leading to the formation of H_2O and *N_2O species. This reaction step is 1.85 and 1.35 eV downward in the ΔG and ΔE profiles, respectively. After H_2O desorption, the remaining N_2O can be similarly removed from the surface due to its low free energy (−0.10 eV). The $C_{59}B$ electrocatalyst is now recovered and ready to begin another NOER cycle. It is important to note that the negative ΔG values for all steps indicated that the NOER process would be spontaneous at high NO coverage under ambient conditions.

3.4 HER process

The HER process is also investigated to evaluate the selectivity of the proposed electrocatalyst. The HER involves the reduction of H^+ ions on the cathode, which results in the formation and evaluation of H_2 molecules ($H^+ + e^- \rightarrow \frac{1}{2}H_2$). The Gibbs free energy diagram for the $H^+ + e^- \rightarrow \frac{1}{2}H_2$ over the $C_{59}B$ is shown in Fig. 7. The adsorption energy of the H atom adsorbed on the B atom of $C_{59}B$ is calculated to be −0.15 eV, which is significantly lower than that of the NO molecule. This shows that the B atom of $C_{59}B$ has a higher affinity for NO molecule adsorption than the H atom. Moreover, the calculated ΔG value derived by the eqn (5) is positive (+0.09 eV), suggesting that the HER process cannot be completed at normal temperature. As a result, in addition to having a high catalytic activity, our proposed electrocatalyst is also selective for the NOER process.

4. Conclusions

To conclude, we evaluated the potential of $C_{59}B$ as an active metal-free electrocatalyst for the NOER process using the DFT methodology. According to the calculated formation energy, a B atom may be stably inserted into the C_{60} fullerene, forming three covalent B–C bonds with the adjacent C atoms. The computed free energy values of each elementary step revealed that *NOH is a major species at low NO molecule coverages and NH_3 is the main product, with the P1-1 route being the favored one with no limiting potential. Furthermore, the efficient interaction of *NOH and NO species can result in the production of the N_2O molecule, which is thermodynamically favored under mild conditions. $C_{59}B$ might be a viable candidate for the NOER based on a set of factors such as high stability, exceptional catalytic activity, free limiting potential, and high performance. Hence, the findings of the current study can be used to design fullerene-based SACs for the electrochemical reduction of NO pollutants.

Conflicts of interest

There are no conflicts to declare.

References

1 J. Lancaster Jr, *Nitric Oxide: Principles and Actions*, Elsevier, 1996.
2 D. A. Vallero, Air Pollution: Atmospheric Wastes, in *Waste*, Academic Press, 2019, pp. 453–475.
3 S. Roy and A. Baiker, *Chem. Rev.*, 2009, **109**, 4054–4091.
4 V. Rosca, M. Duca, M. T. de Groot and M. T. Koper, *Chem. Rev.*, 2009, **109**, 2209–2244.
5 M. Duca and M. T. Koper, *Energy Environ. Sci.*, 2012, **5**, 9726–9742.

6 M. F. Irfan, J. H. Goo and S. D. Kim, *Appl. Catal., B*, 2008, **78**, 267–274.

7 A. A. Verma, S. A. Bates, T. Anggara, C. Paolucci, A. A. Parekh, K. Kamasamudram, A. Yezerets, J. T. Miller, W. N. Delgass and W. F. Schneider, *J. Catal.*, 2014, **312**, 179–190.

8 M. D. Esrafili and N. Saeidi, *Superlattices Microstruct.*, 2015, **81**, 7–15.

9 G. Cheng, X. Liu, X. Song, X. Chen, W. Dai, R. Yuan and X. Fu, *Appl. Catal., B*, 2020, **277**, 119196.

10 X. Song, G. Qin, G. Cheng, W. Jiang, X. Chen, W. Dai and X. Fu, *Appl. Catal., B*, 2021, **284**, 119761.

11 Z. W. Seh, J. Kibsgaard, C. F. Dickens, I. Chorkendorff, J. K. Nørskov and T. F. Jaramillo, *Science*, 2017, **355**, 6321.

12 A. De Vooys, M. Koper, R. Van Santen and J. Van Veen, *J. Catal.*, 2001, **202**, 387–394.

13 I. Katsounaros, M. C. Figueiredo, X. Chen, F. Calle-Vallejo and M. T. Koper, *ACS Catal.*, 2017, **7**, 4660–4667.

14 J. Long, S. Chen, Y. Zhang, C. Guo, X. Fu, D. Deng and J. Xiao, *Angew. Chem.*, 2020, **132**, 9798–9805.

15 S. Yang, J. Kim, Y. J. Tak, A. Soon and H. Lee, *Angew. Chem.*, 2016, **55**, 2058–2062.

16 Y. Qu, Z. Li, W. Chen, Y. Lin, T. Yuan, Z. Yang, C. Zhao, J. Wang, C. Zhao and X. Wang, *Nat. Catal.*, 2018, **1**, 781.

17 J. Gu, C.-S. Hsu, L. Bai, H. M. Chen and X. Hu, *Science*, 2019, **364**, 1091–1094.

18 X. Li, H. Rong, J. Zhang, D. Wang and Y. Li, *Nano Res.*, 2020, **13**, 1842–1855.

19 C. Ling, X. Bai, Y. Ouyang, A. Du and J. Wang, *J. Phys. Chem. C*, 2018, **122**, 16842–16847.

20 D. Ma, Z. Zeng, L. Liu, X. Huang and Y. Jia, *J. Phys. Chem. C*, 2019, **123**, 19066–19076.

21 L. Wang, H. Dong, Z. Guo, L. Zhang, T. Hou and Y. Li, *J. Phys. Chem. C*, 2016, **120**, 17427–17434.

22 Z. Wang, J. Zhao and Q. Cai, *Phys. Chem. Chem. Phys.*, 2017, **19**, 23113–23121.

23 H. He and Y. Jagvaral, *Phys. Chem. Chem. Phys.*, 2017, **19**, 11436–11446.

24 H. Wu, X. Li, R. Zhang and J. Yang, *J. Mater. Chem. A*, 2019, **7**, 3752–3756.

25 X. Lv, W. Wei, P. Zhao, D. Er, B. Huang, Y. Dai and T. Jacob, *J. Catal.*, 2019, **378**, 97–103.

26 Z. Wang, J. Zhao, J. Wang, C. R. Cabrera and Z. Chen, *J. Mater. Chem. A*, 2018, **6**, 7547–7556.

27 Q. Wu, W. Wei, X. Lv, Y. Wang, B. Huang and Y. Dai, *J. Phys. Chem. C*, 2019, **123**, 31043–31049.

28 N. Saeidi, M. D. Esrafili and J. J. Sardroodi, *Appl. Surf. Sci.*, 2021, **544**, 148869.

29 J. Zhang, H. Yang and B. Liu, *Adv. Energy Mater.*, 2021, **11**, 2002473.

30 M. D. Esrafili and P. Mousavian, *Int. J. Quantum Chem.*, 2019, **119**, e25857.

31 D. A. Bulushev, A. D. Nishchakova, S. V. Trubina, O. A. Stonkus, I. P. Asanov, A. V. Okotrub and L. G. Bulusheva, *J. Catal.*, 2021, **402**, 264–274.

32 J. Li and Y. Lu, *Nano Lett.*, 2003, **3**, 929.

33 L. A. Ponomarenko, F. Schedin, M. I. Katsnelson, R. Yang, E. W. Hill, K. S. Novoselov and A. K. Geim, *Science*, 2008, **320**, 356–358.

34 G. Otero, G. Biddau, C. Sánchez-Sánchez, R. Caillard, M. F. López, C. Rogero, F. J. Palomares, N. Cabello, M. A. Basanta and J. Ortega, *Nature*, 2008, **454**, 865.

35 L. Dai, D. W. Chang, J. B. Baek and W. Lu, *Small*, 2012, **8**, 1130–1166.

36 Y. Fujimoto and S. Saito, *J. Appl. Phys.*, 2014, **115**, 153701.

37 Y. Tang, X. Dai, Z. Yang, Z. Liu, L. Pan, D. Ma and Z. Lu, *Carbon*, 2014, **71**, 139–149.

38 D. S. De, J. A. Flores-Livas, S. Saha, L. Genovese and S. Goedecker, *Carbon*, 2018, **129**, 847–853.

39 Y. Zhao, Y.-H. Kim, A. Dillon, M. Heben and S. Zhang, *Phys. Rev. Lett.*, 2005, **94**, 155504.

40 C. H. Woo, B. C. Thompson, B. J. Kim, M. F. Toney and J. M. Fréchet, *J. Am. Chem. Soc.*, 2008, **130**, 16324–16329.

41 Y. He, H.-Y. Chen, J. Hou and Y. Li, *J. Am. Chem. Soc.*, 2010, **132**, 1377–1382.

42 Y. Yuan, S. Han, D. Grozea and Z. H. Lu, *Appl. Phys. Lett.*, 2006, **88**, 093503.

43 J. Shi, H. Zhang, L. Wang, L. Li, H. Wang, Z. Wang, Z. Li, C. Chen, L. Hou and C. Zhang, *Biomaterials*, 2013, **34**, 251–261.

44 Y. Liu, Y. Pu, L. Sun, H. Yao, B. Zhao, R. Zhang and Y. Zhang, *J. Biomed. Nanotechnol.*, 2016, **12**, 1393–1403.

45 S. Bashiri, E. Vessally, A. Bekhradnia, A. Hosseinian and L. Edjlali, *Vacuum*, 2017, **136**, 156–162.

46 J. A. Rather and K. De Wael, *Sens. Actuators, B*, 2013, **176**, 110–117.

47 S. Sutradhar and A. Patnaik, *Sens. Actuators, B*, 2017, **241**, 681–689.

48 M. D. Esrafili and N. Mohammadirad, *Mol. Phys.*, 2017, **115**, 1633–1641.

49 M. K. Hazrati and N. L. Hadipour, *Phys. Lett. A*, 2016, **380**, 937–941.

50 M. Moradi, M. Nouraliei and R. Moradi, *Phys. E*, 2017, **87**, 186–191.

51 R. Bagheri, M. Babazadeh, E. Vessally, M. Es'haghi and A. Bekhradnia, *Inorg. Chem. Commun.*, 2018, **90**, 8–14.

52 M. Ganji and H. Yazdani, *Chin. Phys. Lett.*, 2010, **27**, 043102.

53 C. Ramachandran, *J. Phys. Chem. A*, 2017, **121**, 1708–1714.

54 M. D. Esrafili and S. Heidari, *Comput. Theor. Chem.*, 2019, **1151**, 50–57.

55 M. D. Esrafili and S. Heydari, *ChemistrySelect*, 2019, **4**, 2267–2274.

56 B. Delley, *J. Chem. Phys.*, 1990, **92**, 508–517.

57 B. Delley, *J. Chem. Phys.*, 2000, **113**, 7756–7764.

58 J. P. Perdew, K. Burke and M. Ernzerhof, *Phys. Rev. Lett.*, 1996, **77**, 3865–3868.

59 S. Grimme, *J. Comput. Chem.*, 2006, **27**, 1787–1799.

60 C. Fonseca Guerra, J. W. Handgraaf, E. J. Baerends and F. M. Bickelhaupt, *J. Comput. Chem.*, 2004, **25**, 189–210.

61 J. K. Nørskov, J. Rossmeisl, A. Logadottir, L. Lindqvist, J. R. Kitchin, T. Bligaard and H. Jonsson, *J. Phys. Chem. B*, 2004, **108**, 17886–17892.

62 R. D. Johnson, http://srdata.nist.gov/cccbdb, 2006.

63 A. Klamt and G. Schüürmann, *J. Chem. Soc., Perkin Trans. 2*, 1993, **2**, 799–805.

64 J. K. Nørskov, T. Bligaard, A. Logadottir, J. Kitchin, J. G. Chen, S. Pandelov and U. Stimming, *J. Electrochem. Soc.*, 2005, **152**, J23.

65 Q. Z. Li, J. J. Zheng, J. S. Dang and X. Zhao, *ChemPhysChem*, 2015, **16**, 390–395.

66 Y. Wang, M. Jiao, W. Song and Z. Wu, *Carbon*, 2017, **114**, 393–401.

67 X. Chen, J. Chang and Q. Ke, *Carbon*, 2018, **126**, 53–57.

68 M. D. Esrafili and H. Janebi, *Mol. Phys.*, 2020, **118**, e1631495.

69 M. D. Esrafili, A. A. Khan and P. Mousavian, *RSC Adv.*, 2021, **11**, 22598–22610.

70 Z. Wang, J. Zhao, J. Wang, C. R. Cabrera and Z. Chen, *J. Mater. Chem. A*, 2018, **6**, 7547–7556.

71 S. Ji and J. Zhao, *New J. Chem.*, 2018, **42**, 16346–16353.

72 Q. Wu, W. Wei, X. Lv, Y. Wang, B. Huang and Y. Dai, *J. Phys. Chem. C*, 2019, **123**, 31043–31049.